

1
2
3
4
5
6
7 **Increasing the credibility of regional climate simulations**
8 **by introducing subgrid-scale cloud – radiation interactions**
9

10
11
12
13
14
15 Jerold A. Herwehe*, Kiran Alapaty, Tanya L. Spero, and Christopher G. Nolte

16
17
18 Atmospheric Modeling and Analysis Division, National Exposure Research Laboratory,
19 Office of Research and Development, U.S. Environmental Protection Agency
20 Research Triangle Park, NC 27711, USA
21

22
23
24
25
26
27
28
29
30 Revised 14 April 2014

31
32
33 Submitted to the *Journal of Geophysical Research – Atmospheres*
34
35
36
37
38
39
40
41

42 *Corresponding author. U.S. Environmental Protection Agency, 109 T.W. Alexander Dr., Mail
43 Drop E243-01, Research Triangle Park, NC 27711.

44 Tel.: +1 919 541 0166; fax: +1 919 541 1379.

45 E-mail address: herwehe.jerry@epa.gov (J. Herwehe)
46
47

48 Abstract

49
50 The radiation schemes in the Weather Research and Forecasting (WRF) model have previously
51 not accounted for the presence of subgrid-scale cumulus clouds, thereby resulting in
52 unattenuated shortwave radiation which can lead to overly energetic convection and
53 overpredicted surface precipitation. This deficiency can become problematic when applying
54 WRF as a regional climate model (RCM). Therefore, modifications were made to the WRF
55 model to allow the Kain-Fritsch (KF) convective parameterization to provide subgrid-scale cloud
56 fraction and condensate feedbacks to the Rapid Radiative Transfer Model – Global (RRTMG)
57 shortwave and longwave radiation schemes. The effects of these changes are analyzed via three-
58 year simulations using the standard and modified versions of WRF, comparing the modeled
59 results with the North American Regional Reanalysis (NARR) and Climate Forecast System
60 Reanalysis data, as well as with available data from the Surface Radiation Network and Clouds
61 and Earth’s Radiant Energy System. During the summer period, including subgrid cloudiness
62 estimated by KF in the RRTMG reduces the surface shortwave radiation, leading to less buoyant
63 energy, which is reflected in a smaller diabatic convective available potential energy, thereby
64 alleviating the overly-energetic convection. Overall, these changes have reduced the
65 overprediction of monthly regionally-averaged precipitation during summer for this RCM
66 application; e.g., by as much as 49 mm for the southeastern U.S., to within 0.7% of the NARR
67 value of 221 mm. These code modifications have been incorporated as an option available in the
68 latest version of WRF (v3.6).

69

70 Keywords

71 cumulus parameterization, cloud feedback, radiation budget, regional climate model, WRF

72

73 **1. Introduction**

74

75 Climate change affects air and water quality, as well as human and ecosystem health, and thus,
76 the accuracy of regional climate change projections is critical to develop credible climate change
77 mitigation and adaptation plans. The most important processes in determining the climate and its
78 variability are the interactions between atmospheric radiation, clouds, aerosols, and greenhouse
79 gases [IPCC, 2013; Liang and Zhang, 2013]. Zhang *et al.* [2013b] used the Cloud-Aerosol-
80 Radiation (CAR) ensemble modeling system [Liang and Zhang, 2013] to show that radiative
81 transfer calculations are most sensitive to cloud cover treatment and subgrid-scale cloud
82 variability. For global models, Zhang *et al.* [2013a] found that the structure of the subgrid-scale
83 clouds, such as vertical overlap and horizontal variability, played a dominant role, accounting for
84 40-75% of the total model spreads of cloud radiative effects.

85

86 In global climate models, cloudiness associated with subgrid-scale cumulus convection has been
87 represented by using a prognostic approach [e.g., Tiedtke, 1993] or a diagnostic approach [e.g.,
88 Collins *et al.*, 2004] or a statistical approach using probability density functions [e.g., Bony and
89 Emanuel, 2001; Tompkins, 2002]. Since global models are used for multi-decadal and multi-
90 century climate simulations, inclusion of subgrid-scale convective cloud and radiation
91 interactions are necessary to capture the observed climate variability. The majority of regional
92 modelers use limited area models for numerical weather prediction, where cloud – radiation
93 interactions for deep and shallow subgrid-scale clouds have been regarded as having negligible

94 impacts on forecasting. For regional models, *Kvamstø* [1991] was the first study to introduce
95 convective cloud – radiation interactions by using a variation of the *Xu and Krueger* [1991]
96 formulation. In addition, the National Centers for Environmental Prediction (NCEP) Regional
97 Spectral Model (RSM) uses a formulation to represent convective cloudiness based on *Xu and*
98 *Randall* [1996] for all types of clouds.

99
100 The Weather Research and Forecasting model (WRF) [*Skamarock and Klemp*, 2008] is being
101 used as a regional climate model (RCM) by many groups [e.g., *Georgescu et al.*, 2014; *Bullock*
102 *et al.*, 2013; *Glisan et al.*, 2013; *Harkey and Holloway*, 2013; *Gao et al.*, 2012; *Liang et al.*,
103 2012; *Yang et al.*, 2012; *Argüeso et al.*, 2011; *Bukovsky and Karoly*, 2011]. One finding has
104 been that summer convective systems simulated by WRF are highly energetic, leading to
105 excessive surface precipitation. Our hypothesis is that excessive summertime precipitation
106 predictions occur with WRF, in part, because the model does not consider the interactions
107 between subgrid convective clouds and radiation, thereby omitting an important process that
108 strongly influences the climate. Thus, in model process integration, the subgrid-scale cloudiness
109 associated with convective clouds (from shallow cumuli to deep thunderstorms) does not exist
110 and radiation passes through the atmosphere nearly unimpeded, shining on a surface possibly
111 wetted by convective precipitation, causing more instability in the moist air, and potentially
112 leading to overly energetic convection in a positive feedback loop. As of WRF version 3.5, grid-
113 scale, or resolved, cloudiness is generated only when grid-scale saturation is attained. When
114 modeling at coarse resolutions, grid-scale saturation is difficult to achieve during summer
115 conditions, resulting in WRF-simulated cloudiness appearing only when associated with large
116 mesoscale convective complexes or synoptic-scale frontal systems.

117
118 In a letter by *Alapaty et al.* [2012], the importance of including subgrid-scale convective cloud
119 and radiation interactions on climatological surface precipitation was established. By
120 implementing convective cloud – radiation interactions into the WRF model, they also improved
121 the simulated cloud fields and shortwave (SW) and longwave (LW) radiation variability.
122 However, their study did not provide any analysis of the processes behind the impacts of cloud –
123 radiation interactions on various climate parameters. Therefore, the objective of the present
124 study, which uses the same implementation of subgrid-scale cloudiness – radiation interactions
125 in WRF as *Alapaty et al.* [2012], is to conduct a detailed analysis of several cloud, radiation, and
126 precipitation parameters to examine the impacts of subgrid-scale convective cloud and radiation
127 interactions on regional climate simulations. This effort will help realize the overarching future
128 objective of the research being conducted by our regional climate modeling team at the U.S.
129 Environmental Protection Agency to develop credible ensemble regional climate simulations
130 driven by downscaled results from multiple general circulation models (GCMs).

131

132 **2. Development and Modeling Approach**

133

134 **2.1. Implementation of Subgrid-Scale Cloud – Radiation Interactions**

135

136 GCMs, due to their historically coarse grid resolutions, have long included parameterizations to
137 account for the macrophysics and radiative effects of subgrid-scale convective cloudiness when
138 simulating global climate [e.g., *Lauer and Hamilton, 2013; Yang et al., 2013*]. *Kvamstø* [1993]
139 tested a subgrid cloudiness formulation, originally based on the cloud ensemble modeling study

140 of *Xu and Krueger* [1991], in a mesoscale model and compared it with the Sundqvist [*Sundqvist*,
 141 1988] and relative humidity (RH)-based [*Kvamstø*, 1991] schemes, but the *Xu and Krueger* (*XK*)
 142 formulation outperformed the others. Therefore, an *XK*-based convective cloudiness formulation
 143 that is widely used in GCMs, such as the Community Atmosphere Model (CAM), was
 144 implemented as described by *Alapaty et al.* [2012] into WRF via its Kain-Fritsch (KF)
 145 convective parameterization [*Kain*, 2004] and Rapid Radiative Transfer Model – Global
 146 (RRTMG) SW and LW radiation schemes [*Iacono et al.*, 2008]. In the present WRF RCM
 147 study, cloud updraft mass flux (M_u) at each model level from the KF convective parameterization
 148 was utilized to estimate the subgrid-scale convective cloud cover (A_{sh} and A_{dp}) following the *XK*-
 149 based formulations in CAM3 [*Collins et al.*, 2004], CAM4 [*Neale et al.*, 2010b], and CAM5
 150 [*Neale et al.*, 2010a], where subscript *sh* signifies shallow convective clouds and subscript *dp*
 151 deep convective clouds:

$$152 \quad A_{sh} = k_{1,sh} \ln(1 + k_2 M_{u,sh}) \quad (1)$$

$$153 \quad A_{dp} = k_{1,dp} \ln(1 + k_2 M_{u,dp}) \quad (2)$$

154 Here, as in CAM3, empirical parameters $k_{1,sh} = 0.07$ and $k_{1,dp} = 0.14$, and, for both types of
 155 convective clouds, $k_2 = 500 \text{ m}^2 \text{ s kg}^{-1}$. Following CAM5, these convective cloud fractions were
 156 limited to $A_{sh} \leq 0.2$ and $A_{dp} \leq 0.6$, or 20% and 60%, respectively, of grid cell area. For each
 157 convective updraft, depending on the buoyancy of the updraft, atmospheric conditions, and other
 158 criteria, the KF convective parameterization will produce either deep (precipitating) convection
 159 or shallow (nonprecipitating) convection, but not both in the same grid cell. Therefore, in this
 160 study, KF-based subgrid-scale convective or cumulus (denoted by subscript *cu*) cloudiness in
 161 each grid cell was either

$$162 \quad A_{cu} = A_{sh} \quad (\leq 0.2) \quad (3)$$

163 or

$$164 \quad A_{cu} = A_{dp} \quad (\leq 0.6). \quad (4)$$

165 Horizontal cloud overlap was treated similarly to CAM5, allowing cumulus convection to rise
 166 through and partially displace any existing resolved, or grid-scale, stratus cloud layers, while also
 167 accounting for compensating subsidence around the new convective cloud. Assuming that the
 168 existing grid-scale cloudiness is given by a_{gs} (limited to ≤ 1.0), then the adjusted grid-scale cloud
 169 fraction A_{gs} is determined by accounting for the overriding presence of subgrid cumulus clouds
 170 and their associated compensating subsidence according to CAM5 as in *Neale et al.* [2010a]:

$$171 \quad A_{gs} = (1 - A_{cu}) a_{gs} . \quad (5)$$

172 The new total cloudiness A_{tot} was then determined for each model level and grid cell by summing
 173 the contributions from the adjusted grid-scale cloudiness (A_{gs}) and the subgrid-scale cloudiness
 174 (A_{cu}), or:

$$175 \quad A_{tot} = A_{gs} + A_{cu} \quad (\leq 1.0) \quad (6)$$

176 where again, the total cloud cover cannot exceed unity or 100% of individual grid cell area.

177

178 Fractional cloudiness and cloud condensate (both liquid water and ice) are used by the RRTMG
 179 SW and LW radiation schemes to calculate cloud ice and liquid water paths for the radiative
 180 transfer and attenuation. For consistency, the reduction in the original grid-scale cloudiness due
 181 to intruding convection was accompanied by a corresponding adjustment to the grid-scale cloud
 182 ice and liquid water paths in the RRTMG radiation schemes. Cloud fraction, liquid water and
 183 ice condensate associated with the KF-generated subgrid-scale clouds were also passed to the
 184 RRTMG radiation schemes, where separate subgrid-scale cloud ice and liquid water paths were
 185 calculated and then combined with the grid-scale cloud paths to form new total cloud ice and

186 liquid water paths for radiation attenuation. Thus, in addition to the standard connection between
187 resolved clouds and the radiation budget, the above methodology establishes a link for
188 interactions between the subgrid-scale cumulus clouds and radiation in the WRF model.

189

190 **2.2. Model Configuration for Regional Climate Simulations**

191

192 The new subgrid-scale cloud – radiation interactions implemented into WRF were tested in a
193 regional climate modeling application using WRF version 3.3.1 with the Advanced Research
194 WRF (ARW) core (http://www.mmm.ucar.edu/wrf/users/download/get_sources.html)
195 [Skamarock and Klemp, 2008] for the 3-year period 1988-1990 after a one-month spinup
196 (December 1987). These are the first three years of the 20-year RCM simulations discussed by
197 *Otte et al.* [2012] in a study on extreme values of surface temperature and precipitation, and also
198 by *Bowden et al.* [2013] in a study on the impact of large-scale circulation on those
199 meteorological quantities. Climatologically, the summers of the 1988-1990 period showed
200 interesting interannual variability, with the contiguous U.S. having above normal precipitation
201 (12% higher than the 1971-2000 climatological average) and slightly cooler mean temperatures
202 (-0.16°C cooler than 1971-2000) during the summer of 1989, flanked by the generally drier,
203 hotter summers of 1988 and 1990 (<http://www.ncdc.noaa.gov/cag/data-info>). For the Southeast
204 region, the summer of 1989 was on the order of 1°C cooler, while precipitation was around 30%
205 above normal, primarily due to the late June landfall of Tropical Storm Allison arriving from the
206 western Gulf of Mexico.

207

208 The model domain configuration in the present work matched those of the *Otte et al.* [2012] and
209 *Bowden et al.* [2013] studies, covering much of North America and all of the contiguous United
210 States with two-way nested grids of 108 km and 36 km horizontal spacing, respectively (see
211 Figure 1 in *Bowden et al.* [2012]), with 34 model layers extending up to 50 hPa. As in those
212 efforts, initial and lateral boundary conditions in this RCM study came from the NCEP –
213 Department of Energy (DOE) Atmospheric Model Intercomparison Project (AMIP-II) reanalysis
214 (R-2) data (<http://www.esrl.noaa.gov/psd/data/gridded/data.ncep.reanalysis2.html>) [*Kanamitsu et*
215 *al.*, 2002] downscaled from its T62 spectral model grid (1.875° at the equator) and chosen as a
216 proxy for GCM fields. Four-dimensional data assimilation (FDDA) was enabled for the 3-year
217 WRF simulations, using R-2 data to steer the interior fields via analysis nudging of winds,
218 temperature, and moisture above the boundary layer, using the same nudging coefficient
219 strengths as reported in *Otte et al.* [2012]. A discussion of the use of nudging for RCM
220 applications is given in *Otte et al.* [2012]. Observational data, other than that already
221 incorporated into the R-2 data set, were not included in the FDDA of this study.

222
223 Primary WRF model physics options chosen for the 3-year RCM simulations include the Noah
224 land surface model (LSM) [*Chen and Dudhia*, 2001], the Yonsei University (YSU) planetary
225 boundary layer (PBL) scheme [*Hong et al.*, 2006], the WRF single-moment 6-class (WSM6)
226 microphysics scheme [*Hong and Lim*, 2006], and the aforementioned KF convective
227 parameterization and RRTMG SW and LW radiation schemes. For the nested 36 km domain,
228 the radiation calculations were updated every 15 minutes during the simulation, while the
229 convective parameterization checked every time step (2.5 minutes) to determine whether the
230 atmospheric conditions were sufficient to generate convective cloud formation over a particular

231 location. These options are the same as those used by *Otte et al.* [2012] and are common choices
232 in WRF-based regional climate studies at grid sizes comparable to the 36 km grids used here.

233

234 For the present study, two different regional climate simulations were conducted and evaluated
235 against available observations: 1) the **Base** case, which used the standard KF and RRTMG
236 schemes available with the release version of WRF, and 2) the **Modified** case, in which the KF
237 convective parameterization and the RRTMG SW and LW radiation schemes were modified as
238 described in Section 2.1 to account for the interaction of subgrid-scale cumulus clouds with the
239 SW and LW radiation. Note that though the Base case does not include subgrid-scale cloudiness
240 effects on radiation, the resolved (grid-scale) cloudiness can exhibit partial cloud fractions
241 between 0 and 1 depending upon the grid-scale relative humidity, as based on the original
242 algorithm of *Xu and Randall* [1996].

243

244 **3. Regional Climate Simulation Results and Evaluation**

245

246 Analysis of the RCM simulations and comparison with observational and reanalysis data sets
247 were conducted utilizing averages over several temporal ranges, such as monthly and seasonal,
248 as well as annual and diurnal cycles. These temporal averages currently include *all* hours for
249 each day; therefore, the signal for any process or variable that is strongly dependent on daytime
250 solar heating will be diminished by the inclusion of nocturnal values in the averages. Areal
251 averaging, over land cells only, was also performed in order to elucidate any regional
252 dependence of the results. Analysis in this study was only performed on the 36-km domain.

253

254 Dilute or diabatic convective available potential energy (dCAPE), as its name implies, is the
255 calculation of CAPE based on an ascending air parcel that entrains environmental air [*Kain*,
256 2004]. Values for dCAPE are equivalent to the available buoyant energy (ABE) within the
257 cumulus cloud generated by the KF convective parameterization. Typical dCAPE values range
258 up to 800 J kg^{-1} and are considerably less than the values for the more commonly diagnosed
259 undiluted or adiabatic CAPE which are on the order of several thousand J kg^{-1} ; an example of
260 this difference is illustrated in *Zhang* [2009] using data from the Tropical Warm Pool
261 International Cloud Experiment (TWP-ICE) field study. As previously mentioned, the radiation
262 schemes in standard WRF do not consider subgrid-scale cumulus clouds, thereby leading to
263 overly energetic convection in places where the solar radiation shines through the radiatively-
264 passive cumulus clouds to surfaces which may be wet from convective precipitation. Including
265 the subgrid cumulus cloud interactions with radiation in the Modified case shades the surface at
266 the appropriate locations, reducing the heat energy available for convection.

267
268 Figure 1 shows this effect on dCAPE for the June-July-August (JJA) 1989 summer average. As
269 noted above, these three-month averages are based on all hourly values, including nocturnal
270 values when dCAPE is typically small to zero, thus resulting in a considerable reduction in
271 magnitude compared to the order-of-magnitude larger hourly instantaneous dCAPE values.
272 Nevertheless, the relatively large average dCAPE values over land in the Southeast U.S.
273 (hereafter, SE) for the Base case (Figure 1a) are substantially reduced in the Modified case
274 (Figure 1b) by up to 50% in many areas (Figure 1c). Analogous reductions in dCAPE were also
275 seen in the simulation results for the summers of 1988 and 1990. Lower dCAPE values signify
276 less energy available for convective development, thus appearing to mitigate the overly energetic

277 convection produced by WRF in the Base case. Scattered small increases in dCAPE are seen
278 over the warm water of the Gulf of Mexico and the western Atlantic Ocean in Figure 1c. The sea
279 surface temperatures (SSTs) are prescribed and identical for the Base and Modified cases, but an
280 examination of the 1989 JJA atmospheric temperatures below 500 hPa over these ocean areas
281 revealed a slight warming (up to around 0.1 K at 2-m height over the western Atlantic) in the
282 Modified case, thereby slightly increasing atmospheric instability. Disregarding the strong
283 convective activity over the mountains of the Mexican Sierra Madre Occidental in Figures 1a-b,
284 these dCAPE differences (Figure 1c) indicate significant reductions in simulated energy
285 available for convective development in the SE. As will be shown later, the summer of 1989 is
286 noteworthy because of the considerable wet bias in the Base case and the subsequent
287 improvement when including subgrid cloudiness effects on radiation.

288
289 Compared with the Base case, the Modified case slightly reduced cloud fraction above 300 hPa
290 (Figure 2a), but generally increased summertime cloud fraction over land areas below 300 hPa
291 (Figures 2b-d). Due to the addition of subgrid-scale cloudiness, most of the increase in total
292 cloudiness occurs in the middle layer (Figure 2c) in accordance with convective cloud process
293 dynamics. The bulk layer cloud fraction differences shown in Figure 2 are based on the
294 maximum cloud fraction found in the several model layers contained within that bulk layer for
295 each horizontal grid cell, with the Modified – Base differences then computed and averaged over
296 the three-month period. To assess the relative magnitude of these changes in cloud fraction,
297 example values of 1989 JJA cloud fraction over land from the Modified case are: for the very
298 high layer, a large area of 0.7-0.8 cloud fractions over the SE; for the high layer, maximum
299 values of 0.2-0.3 located over the eastern U.S.; for the middle layer, a maximum of up to 0.14

300 over the Appalachian Mountains up to New England; and for the low layer, maximum values up
301 to 0.5 over West Virginia and along the Appalachians. The large cloud fractions in the very high
302 layer are from glaciated anvil tops of deep cumulonimbus generated by summer convection in
303 the SE. Over the relatively cool water of the eastern Pacific Ocean, implementing cumulus cloud
304 – radiation interactions reduced the persistent low-level marine stratocumulus (Figure 2d) by up
305 to 10% over many areas from Base case cloud fraction values of 0.7-0.9. This reduction of cloud
306 fraction over water is due to new shallow-convection cumulus (limited to a maximum of 20% of
307 grid cell area) partially displacing any existing resolved or grid-scale marine stratocumulus
308 (which originally covered up to 100% of grid cell area) and clearing part of these affected grid
309 cells via compensating subsidence (Eq. 5). Over the warm water of the Gulf of Mexico (with
310 1989 JJA Base case low-layer cloud fraction maximums of 0.2-0.35) and western Atlantic Ocean
311 (with 1989 JJA Base case low-layer cloud fractions of 0.3-0.6), the Modified case showed a
312 different response by increasing the cloud cover in the high and middle layers (Figures 2b and c)
313 above the decreased cloudiness in the low cloud layer (Figure 2d). Though convection over
314 water is not as strong as that over land, the relatively warm SSTs in these areas still initiate deep
315 convection, partially displacing the near-surface grid-scale clouds while adding subgrid-scale
316 cloudiness primarily to the middle and high cloud layers.

317
318 Figures 1 and 2 establish the SE as this study's region of interest for evaluating the influence of
319 the subgrid-scale cumulus cloud – radiation interactions. Here, the SE region is defined as the
320 same latitude-longitude rectangular area (29-38°N and 75-95°W) used by *Bowden et al.* [2012]
321 and shown in their Figure 1. All regional areal averaging in the present study was performed for

322 land cells only in order to enhance the signal response from cloud – radiation interactions during
323 convection.

324

325 Satellite-based observations of cloudiness were obtained from the Clouds and the Earth's
326 Radiant Energy System (CERES) [*Smith et al.*, 2011] data set, available for the March 2000
327 through October 2005 period. Because the CERES time period does not match the WRF RCM
328 simulation period of this study, a qualitative climatological comparison was made. Figure 3
329 shows monthly averages of cloud fraction for the SE computed over the time periods available
330 from each data set (i.e., five years and eight months for CERES and three years for the RCM
331 simulations). The Modified case appropriately increased the cloud fractions in May, June, July,
332 and August toward the average CERES values for the high (500-300 hPa; Figure 3a), middle
333 (700-500 hPa; Figure 3b), and low (surface – 700 hPa; Figure 3c) cloud layers, with the most
334 pronounced improvement in the middle layer (Figure 3b) consistent with the deep convection of
335 summer. Both RCM simulations overpredicted the very high (above 300 hPa) cloud fractions
336 year-round, especially during summer (not shown). Also evident in Figure 3 is a general
337 overprediction of cloudiness by WRF at all levels during the winter months, which was not
338 expected to be improved by the changes introduced in the Modified case.

339

340 Observations of various components of the atmospheric radiation budget are also available as
341 part of the CERES data. The addition of the subgrid-scale cloudiness in the Modified case had
342 the anticipated effect of decreasing the SW downwelling radiation at the surface (Figure 4a) and
343 increasing the SW upwelling at the top of the atmosphere (TOA) (Figure 4b) to produce more
344 agreement, in a climatological sense, with the CERES data. The additional cumulus cloudiness

345 had a relatively minor effect (0.4-1.6 W m⁻²) on the LW radiation (not shown), with a slight
346 decrease in LW upwelling at TOA and a slight increase in LW downwelling at the surface.
347
348 Surface SW radiation from the RCM simulations is also compared with the North American
349 Regional Reanalysis (NARR). The NARR data set (<http://rda.ucar.edu/datasets/ds608.0/>;
350 <http://www.emc.ncep.noaa.gov/mmb/rrean/>) [Mesinger *et al.*, 2006], at 32-km horizontal grid
351 spacing with 45 layers, is a product of the NCEP Eta model incorporating direct assimilation of
352 radiances and precipitation observations, among other measurements. Figure 5 shows that
353 including the cumulus cloud – radiation interactions in the Modified case improved the simulated
354 SW downwelling radiation at the surface during the warm season in the SE as seen in the three-
355 year monthly time series (Figure 5a) and during the daytime hours as shown in the June 1989
356 averaged diurnal cycle (Figure 5b). The Base case does not simulate enough cloudiness, leading
357 to an overestimation of monthly-averaged surface SW radiation of up to 20-40 W m⁻² in summer
358 months, a substantial amount. On an hourly scale (Figure 5b), this translates to an
359 overestimation of 80-100 W m⁻² for the incident SW radiation, leading to overprediction of
360 summertime heating and precipitation, two fields of great interest for climate change
361 applications.

362
363 Additional data suitable for comparison with the simulated surface SW downwelling radiation
364 are observations from the Surface Radiation Network (SURFRAD) [Augustine *et al.*, 2005]. As
365 with the CERES data, the SURFRAD observations are from a different time period than the
366 RCM simulations, so a qualitative climatological comparison with the 1988-1990 RCM results
367 was conducted. SURFRAD observations from 1995-2010 were processed to produce an average

368 annual cycle of monthly values for each of the seven SURFRAD measurement sites, two of
369 which are shown in Figure 6. The increased cloudiness present in the Modified case over eastern
370 Colorado shown previously in Figures 2b and 2c is reflected in the improved surface SW
371 downwelling at Table Mountain, Colorado, in Figure 6a. The surface SW downwelling is
372 improved by $\sim 50 \text{ W m}^{-2}$ in summertime when convection is most active. At this site, the
373 normalized mean bias (NMB) for the Modified case is 10.3%, much better than the NMB of
374 20.9% for surface SW radiation from the Base simulation. An improvement in surface SW
375 downwelling of $\sim 20 \text{ W m}^{-2}$ in summer can be seen for the Modified case (NMB=17.6%) when
376 compared with the Base case (NMB=22.6%) at Goodwin Creek, Mississippi (Figure 6b), the
377 lone SURFRAD site in the SE.

378
379 Various effects from the addition of subgrid-scale cloudiness on two-meter temperature (T_{2m}) are
380 shown in Figure 7. Here, as in the [Otte *et al.*, 2012] study, the RCM temperatures are compared
381 with data from the Climate Forecast System Reanalysis (CFSR), which are available at hourly
382 intervals (<http://rda.ucar.edu/datasets/ds093.1/>) [Saha *et al.*, 2010]. The CFSR is a third
383 generation reanalysis product with high-resolution global coverage, based on a coupled
384 atmosphere-ocean-land surface-sea ice system which accounts for changing CO_2 , trace gases,
385 aerosols, and solar variations (Climate Data Guide; [https://climatedataguide.ucar.edu/climate-](https://climatedataguide.ucar.edu/climate-data/climate-forecast-system-reanalysis-cfsr)
386 [data/climate-forecast-system-reanalysis-cfsr](https://climatedataguide.ucar.edu/climate-data/climate-forecast-system-reanalysis-cfsr)). Wang *et al.* [2011] evaluated the 2-m
387 temperatures from CFSR and found that they were more highly correlated with the Global
388 Historical Climatology Network version 2 and the Climate Anomaly Monitoring System
389 (GHCNCAMS) observations and produced better interannual variability and long-term trend
390 than previous NCEP reanalyses (R-1 and R-2). Monthly-averaged simulated T_{2m} values from the

391 Base and Modified cases are in nearly complete agreement (within ± 0.1 K) and are always
392 within ± 1.5 K from CFSR for the SE (not shown). The average diurnal cycle of T_{2m} for June
393 1989 (Figure 7a) reveals the Modified case improvement during afternoon convective conditions,
394 reflecting the influence of fair weather cumulus clouds. Despite the fact that by not segregating
395 cloudy grid cells from clear grid cells when computing the averages inevitably leads to a
396 reduction of the signal, an afternoon difference of over 0.3 K between the Base and Modified
397 cases is still evident (Figure 7a). The additional cloudiness due to accounting for the subgrid-
398 scale cumulus clouds in the Modified case has improved the prediction of extreme heat events
399 (Figure 7b). This occurs because the solar radiation is no longer transmitting through
400 radiatively-passive subgrid-scale clouds to a surface recently wetted by convective precipitation
401 and causing evaporative cooling as in the Base case. Instead, in the Modified case, wet surfaces
402 are now usually shaded by clouds and whenever clear-sky solar radiation reaches the surface, the
403 surface is usually dry, hence producing warmer average near-surface temperatures in
404 summertime.

405
406 Changes in the amount of surface moisture and its heating lead to modification of the Bowen
407 ratio via changes in the latent heat (LH) flux. The effects of subgrid-scale clouds on sensible
408 heat flux were on the order of 10% or less for summer averages, but the effects on latent heat
409 were more substantial and are tied to precipitation changes to be shown later. Figure 8 shows
410 modeled LH compared with the NARR latent heat reanalysis data. Latent heat is a diagnosed
411 quantity and the uncertainty associated with LH values in NARR is unclear, but NARR
412 precipitation is constrained by assimilated precipitation observations which have been converted
413 to latent heat [Mesinger *et al.*, 2006], so the relationship between precipitation and latent heat

414 within NARR is robust. *Otte et al.* [2012] cited several studies which confirmed the close match
415 between NARR precipitation and observations. *Luo et al.* [2007] evaluated NARR land surface
416 and near-surface variables to find that the NARR hydrologic cycle has relatively small residuals
417 for most basins. For the summer of 1989, the Base case shows substantial LH in the eastern half
418 of the U.S. (Figure 8a), while the Modified case (Figure 8b) reduced the LH in that area
419 considerably, by 20% or more (Figure 8c). The LH from the Modified case (Figure 8b) is in
420 better agreement with NARR (Figure 8d), especially over the SE U.S. The significant
421 improvement in average LH flux by the Modified simulation for the summer of 1989 can be seen
422 in the three-year monthly time series for the SE region (Figure 8e), with similar improvements
423 for the summers of 1988 and 1990. A corresponding improvement in afternoon LH flux can be
424 seen in the June 1989 average diurnal cycle in Figure 8f.

425
426 This evidence of changes in the surface moisture budget in the SE can also be seen in the soil
427 moisture values from the Noah LSM. The monthly-averaged time series of aggregated (10 cm –
428 2 m) volumetric deep soil moisture from the Base and Modified cases is illustrated in Figure 9
429 for the SE. Simulating deep soil moisture requires considerable spin-up time to reach a quasi-
430 equilibrium state. Nevertheless, Figure 9 shows that including the subgrid-scale cumulus –
431 radiation interactions reduced the deep soil moisture compared to the Base case after seven
432 months of integration (counting the December 1987 month simulated to spin-up WRF), and the
433 difference between the two cases persists and is greatest during the summer convective season.

434
435 The addition of the subgrid-scale cloud – radiation interactions in the Modified case significantly
436 improved total precipitation during summer when compared with the NARR data, while having,

437 as expected, little to no effect on the cool season precipitation (Figure 10a). It follows that the
438 majority of the improvements seen in the previously discussed simulated fields occurs due to a
439 decrease in convective precipitation in the Modified case (Figure 10b), with additional small
440 contributions to the improvement from the resolved, or grid-scale, precipitation changes (not
441 shown). Summertime deep cumulus convection is usually associated with larger precipitation
442 amounts, evident for the > 1.0 inch threshold statistic in Figure 10c revealing the significant
443 improvement in the Modified case. Much less improvement was seen in the Modified case when
444 including the frequency of light-rain events, with light precipitation in the Modified case
445 behaving similarly to the Base case.

446

447 **4. Summary and Conclusions**

448

449 Regional climate models, such as the WRF model, are used to study the impacts of climate
450 change on regional air quality, ecosystems, and human health. However, until recently, the WRF
451 model lacked a connection between the parameterized subgrid-scale convective clouds and the
452 radiation budget, resulting in simulations with too little cloudiness, but with excessive convective
453 precipitation during mid-latitude summers. To assuage such problems in WRF, [Alapaty *et al.*
454 [2012]] implemented changes in the WRF model that allow the KF convective parameterization
455 to provide subgrid-scale cloud fraction and condensate feedback to the RRTMG SW and LW
456 radiation schemes, utilizing a methodology from the CAM global model. The present study built
457 upon that work by applying the modified WRF to multiyear regional climate simulations over the
458 contiguous U.S. and evaluating the results via comparison with reanalysis and observational data
459 sets.

460
461 Based upon evaluation of the three-year simulations conducted with WRF in this study,
462 implementation of the interaction between the subgrid-scale clouds and the radiation schemes
463 produced the following improvements: additional summer cloudiness, in better agreement with
464 observations; less diabatic CAPE and latent heat flux to reduce the previously overly-energetic
465 convection; reduced overprediction of summer precipitation in the SE, with improved prediction
466 of extreme rainfall events; and improved prediction of extreme heat in the SE. The WRF code
467 changes necessary to make the cumulus – radiation connection are relatively minor, so the
468 aforementioned improvements are achieved with a negligible impact on computation time.

469
470 A future direction for this research is to conduct a more direct evaluation with existing
471 measurements (such as the CERES and SURFRAD data) by simulating analogous years covered
472 in the observations. Additional follow-on research will apply these WRF KF-RRTMG
473 modifications to longer (e.g., multi-decadal) regional climate simulations of the recent past, plus
474 a range of future climate scenarios. We have successfully implemented and tested the subgrid-
475 scale cloud – radiation interactions in newer versions of WRF (specifically, v3.4.1, v3.5, and
476 v3.6 Beta2), with all versions producing similar improvements to the regional climate
477 simulations as reported in this study. The model changes needed to implement the KF
478 cloudiness and RRTMG radiation interactions have been tested by independent groups and will
479 be released by the National Center for Atmospheric Research in April 2014 to benefit the WRF
480 user community.

481

482 **Acknowledgements**

483 We would like to thank Jim Godowitch and Rohit Mathur (U.S.
484 EPA/ORD/NERL/AMAD) for providing technical feedback on this paper. We thank the three
485 anonymous reviewers whose constructive comments helped enhance this paper. We would also
486 like to thank Martin Otte (formerly at U.S. EPA/ORD/NERL/AMAD) for acquiring and
487 processing the CERES data used in this study
488 (http://ceres.larc.nasa.gov/science_information.php). NCEP-DOE Reanalysis 2 (R-2) data were
489 acquired from the National Oceanic and Atmospheric Administration (NOAA) National
490 Operational Model Archive and Distribution System at http://nomad1.ncep.noaa.gov/ncep_data/.
491 SURFRAD data were obtained from the NOAA Earth System Research Laboratory Global
492 Monitoring Division at www.esrl.noaa.gov/gmd/grad/surfrad.

493 Although this paper has been reviewed and approved for publication by the U.S.
494 Environmental Protection Agency, it does not reflect the views and policies of the Agency.

495

496 **References**

497

- 498 Alapaty, K., J. A. Herwehe, T. L. Otte, C. G. Nolte, O. R. Bullock, M. S. Mallard, J. S. Kain, and
499 J. Dudhia (2012), Introducing subgrid-scale cloud feedbacks to radiation for regional
500 meteorological and climate modeling, *Geophysical Research Letters*, 39(24), L24808,
501 doi:10.1029/2012gl054031.
- 502 Argüeso, D., J. M. Hidalgo-Muñoz, S. R. Gámiz-Fortis, M. J. Esteban-Parra, J. Dudhia, and Y.
503 Castro-Díez (2011), Evaluation of WRF Parameterizations for Climate Studies over
504 Southern Spain Using a Multistep Regionalization, *Journal of Climate*, 24(21), 5633-
505 5651, doi:10.1175/JCLI-D-11-00073.1.

- 506 Augustine, J. A., G. B. Hodges, C. R. Cornwall, J. J. Michalsky, and C. I. Medina (2005), An
507 update on SURFRAD—The GCOS surface radiation budget network for the continental
508 United States, *Journal of Atmospheric and Oceanic Technology*, 22(10), 1460-1472,
509 doi:10.1175/JTECH1806.1.
- 510 Bony, S., and K. A. Emanuel (2001), A Parameterization of the Cloudiness Associated with
511 Cumulus Convection; Evaluation Using TOGA COARE Data, *Journal of the*
512 *Atmospheric Sciences*, 58(21), 3158-3183, doi:10.1175/1520-
513 0469(2001)058<3158:APOTCA>2.0.CO;2.
- 514 Bowden, J. H., C. G. Nolte, and T. L. Otte (2013), Simulating the impact of the large-scale
515 circulation on the 2-m temperature and precipitation climatology, *Climate Dynamics*,
516 40(7-8), 1903-1920, doi:10.1007/s00382-012-1440-y.
- 517 Bowden, J. H., T. L. Otte, C. G. Nolte, and M. J. Otte (2012), Examining interior grid nudging
518 techniques using two-way nesting in the WRF model for regional climate modeling,
519 *Journal of Climate*, 25(8), 2805-2823, doi:10.1175/jcli-d-11-00167.1.
- 520 Bukovsky, M. S., and D. J. Karoly (2011), A Regional Modeling Study of Climate Change
521 Impacts on Warm-Season Precipitation in the Central United States*, *Journal of Climate*,
522 24(7), 1985-2002, doi:10.1175/2010JCLI3447.1.
- 523 Bullock, O. R., K. Alapaty, J. A. Herwehe, M. S. Mallard, T. L. Otte, R. C. Gilliam, and C. G.
524 Nolte (2013), An Observation-Based Investigation of Nudging in WRF for Downscaling
525 Surface Climate Information to 12-km Grid Spacing, *Journal of Applied Meteorology*
526 *and Climatology*, 53(1), 20-33, doi:10.1175/JAMC-D-13-030.1.
- 527 Chen, F., and J. Dudhia (2001), Coupling an advanced land surface–hydrology model with the
528 Penn State–NCAR MM5 modeling system. Part I: Model implementation and sensitivity,

- 529 *Monthly Weather Review*, 129(4), 569-585, doi:10.1175/1520-
530 0493(2001)129<0569:CAALSH>2.0.CO;2.
- 531 Collins, W. D., et al. (2004), Description of the NCAR Community Atmosphere Model (CAM
532 3.0)Rep. NCAR/TN-464+STR, 214 pp, National Center for Atmospheric Research.
- 533 Gao, Y., J. S. Fu, J. B. Drake, Y. Liu, and J. F. Lamarque (2012), Projected changes of extreme
534 weather events in the eastern United States based on a high resolution climate modeling
535 system, *Environmental Research Letters*, 7(4), 044025.
- 536 Georgescu, M., P. E. Morefield, B. G. Bierwagen, and C. P. Weaver (2014), Urban adaptation
537 can roll back warming of emerging megapolitan regions, *Proceedings of the National*
538 *Academy of Sciences*.
- 539 Glisan, J. M., W. J. Gutowski, J. J. Cassano, and M. E. Higgins (2013), Effects of Spectral
540 Nudging in WRF on Arctic Temperature and Precipitation Simulations, *Journal of*
541 *Climate*, 26(12), 3985-3999, doi:10.1175/JCLI-D-12-00318.1.
- 542 Harkey, M., and T. Holloway (2013), Constrained dynamical downscaling for assessment of
543 climate impacts, *Journal of Geophysical Research: Atmospheres*, 118(5), 2136-2148,
544 doi:10.1002/jgrd.50223.
- 545 Hong, S.-Y., and J.-O. J. Lim (2006), The WRF single-moment 6-class microphysics scheme
546 (WSM6), *Journal of the Korean Meteorological Society*, 42, 129-151.
- 547 Hong, S.-Y., Y. Noh, and J. Dudhia (2006), A new vertical diffusion package with an explicit
548 treatment of entrainment processes, *Monthly Weather Review*, 134(9), 2318-2341,
549 doi:10.1175/MWR3199.1.
- 550 Iacono, M. J., J. S. Delamere, E. J. Mlawer, M. W. Shephard, S. A. Clough, and W. D. Collins
551 (2008), Radiative forcing by long-lived greenhouse gases: Calculations with the AER

- 552 radiative transfer models, *Journal of Geophysical Research*, 113(D13), D13103,
553 doi:10.1029/2008jd009944.
- 554 IPCC (2013), Climate Change 2013: The Physical Science Basis, Contribution of Working
555 Group I to the Fifth Assessment Report of the Intergovernmental Panel on Climate
556 Change [Stocker, T. F., D. Qin, G.-K. Plattner, M. M. B. Tignor, S. K. Allen, J.
557 Boschung, A. Nauels, Y. Xia, V. Bex, and P. M. Midgley (eds.)], 1535 pp, Cambridge
558 University Press, Cambridge, United Kingdom, and New York, NY, USA. Available at:
559 <http://www.climatechange2013.org/report/>.
- 560 Kain, J. S. (2004), The Kain–Fritsch convective parameterization: An update, *Journal of Applied*
561 *Meteorology*, 43(1), 170-181, doi:10.1175/1520-
562 0450(2004)043<0170:TKCPAU>2.0.CO;2.
- 563 Kanamitsu, M., W. Ebisuzaki, J. Woollen, S.-K. Yang, J. J. Hnilo, M. Fiorino, and G. L. Potter
564 (2002), NCEP–DOE AMIP-II Reanalysis (R-2), *Bulletin of the American Meteorological*
565 *Society*, 83(11), 1631-1643, doi:10.1175/bams-83-11-1631.
- 566 Kvamstø, N. G. (1991), An investigation of diagnostic relations between stratiform fractional
567 cloud cover and other meteorological parameters in numerical weather prediction models,
568 *Journal of Applied Meteorology*, 30(2), 200-216, doi:10.1175/1520-
569 0450(1991)030<0200:AIODRB>2.0.CO;2.
- 570 Kvamstø, N. G. (1993), An investigation of the cumulus cloudiness parameterization in northerly
571 flows in the Norwegian Sea, *Monthly Weather Review*, 121(5), 1434-1449,
572 doi:10.1175/1520-0493(1993)121<1434:aiotcc>2.0.co;2.

- 573 Lauer, A., and K. Hamilton (2013), Simulating clouds with global climate models: A comparison
574 of CMIP5 results with CMIP3 and satellite data, *Journal of Climate*, 26(11), 3823-3845,
575 doi:10.1175/jcli-d-12-00451.1.
- 576 Liang, X.-Z., et al. (2012), Regional Climate–Weather Research and Forecasting Model, *Bulletin*
577 *of the American Meteorological Society*, 93(9), 1363-1387, doi:10.1175/bams-d-11-
578 00180.1.
- 579 Liang, X. Z., and F. Zhang (2013), The cloud–aerosol–radiation (CAR) ensemble modeling
580 system, *Atmos. Chem. Phys.*, 13(16), 8335-8364, doi:10.5194/acp-13-8335-2013.
- 581 Luo, Y., E. H. Berbery, K. E. Mitchell, and A. K. Betts (2007), Relationships between Land
582 Surface and Near-Surface Atmospheric Variables in the NCEP North American Regional
583 Reanalysis, *Journal of Hydrometeorology*, 8(6), 1184-1203, doi:10.1175/2007jhm844.1.
- 584 Mesinger, F., et al. (2006), North American Regional Reanalysis, *Bulletin of the American*
585 *Meteorological Society*, 87(3), 343-360, doi:10.1175/BAMS-87-3-343.
- 586 Neale, R. B., et al. (2010a), Description of the NCAR Community Atmosphere Model (CAM
587 5.0)Rep. NCAR/TN-486+STR, 268 pp, National Center for Atmospheric Research.
- 588 Neale, R. B., et al. (2010b), Description of the NCAR Community Atmosphere Model (CAM
589 4.0)Rep. NCAR/TN-485+STR, 212 pp, National Center for Atmospheric Research.
- 590 Otte, T. L., C. G. Nolte, M. J. Otte, and J. H. Bowden (2012), Does nudging squelch the
591 extremes in regional climate modeling?, *Journal of Climate*, 25(20), 7046-7066,
592 doi:10.1175/jcli-d-12-00048.1.
- 593 Saha, S., et al. (2010), The NCEP Climate Forecast System Reanalysis, *Bulletin of the American*
594 *Meteorological Society*, 91(8), 1015-1057, doi:10.1175/2010BAMS3001.1.

- 595 Skamarock, W. C., and J. B. Klemp (2008), A time-split nonhydrostatic atmospheric model for
596 weather research and forecasting applications, *Journal of Computational Physics*, 227(7),
597 3465-3485, doi:DOI: 10.1016/j.jcp.2007.01.037.
- 598 Smith, G. L., K. J. Priestley, N. G. Loeb, B. A. Wielicki, T. P. Charlock, P. Minnis, D. R.
599 Doelling, and D. A. Rutan (2011), Clouds and Earth Radiant Energy System (CERES), a
600 review: Past, present and future, *Advances in Space Research*, 48(2), 254-263,
601 doi:http://dx.doi.org/10.1016/j.asr.2011.03.009.
- 602 Sundqvist, H. (1988), Parameterization of condensation and associated clouds in models for
603 weather prediction and general circulation simulation, in *Physically-Based Modelling and*
604 *Simulation of Climate and Climatic Change*, edited by M. E. Schlesinger, pp. 433-461,
605 Springer Netherlands, doi:10.1007/978-94-009-3041-4_10.
- 606 Tiedtke, M. (1993), Representation of Clouds in Large-Scale Models, *Monthly Weather Review*,
607 121(11), 3040-3061, doi:10.1175/1520-0493(1993)121<3040:ROCILS>2.0.CO;2.
- 608 Tompkins, A. M. (2002), A Prognostic Parameterization for the Subgrid-Scale Variability of
609 Water Vapor and Clouds in Large-Scale Models and Its Use to Diagnose Cloud Cover,
610 *Journal of the Atmospheric Sciences*, 59(12), 1917-1942, doi:10.1175/1520-
611 0469(2002)059<1917:APPFTS>2.0.CO;2.
- 612 Wang, W., P. Xie, S.-H. Yoo, Y. Xue, A. Kumar, and X. Wu (2011), An assessment of the
613 surface climate in the NCEP climate forecast system reanalysis, *Climate Dynamics*,
614 37(7), 1601-1620, doi:10.1007/s00382-010-0935-7.
- 615 Xu, K.-M., and S. K. Krueger (1991), Evaluation of cloudiness parameterizations using a
616 cumulus ensemble model, *Monthly Weather Review*, 119(2), 342-367, doi:10.1175/1520-
617 0493(1991)119<0342:EOCPUA>2.0.CO;2.

- 618 Xu, K.-M., and D. A. Randall (1996), A Semiempirical Cloudiness Parameterization for Use in
619 Climate Models, *Journal of the Atmospheric Sciences*, 53(21), 3084-3102,
620 doi:10.1175/1520-0469(1996)053<3084:ASCPFU>2.0.CO;2.
- 621 Yang, B., et al. (2013), Uncertainty quantification and parameter tuning in the CAM5 Zhang-
622 McFarlane convection scheme and impact of improved convection on the global
623 circulation and climate, *Journal of Geophysical Research: Atmospheres*, 118(2), 395-
624 415, doi:10.1029/2012jd018213.
- 625 Yang, B., Y. Qian, G. Lin, R. Leung, and Y. Zhang (2012), Some issues in uncertainty
626 quantification and parameter tuning: a case study of convective parameterization scheme
627 in the WRF regional climate model, *Atmospheric Chemistry and Physics*, 12(5), 2409-
628 2427, doi:10.5194/acp-12-2409-2012.
- 629 Zhang, F., X.-Z. Liang, J. Li, and Q. Zeng (2013a), Dominant roles of subgrid-scale cloud
630 structures in model diversity of cloud radiative effects, *Journal of Geophysical Research:*
631 *Atmospheres*, 118(14), 7733-7749, doi:10.1002/jgrd.50604.
- 632 Zhang, F., X.-Z. Liang, Q. Zeng, Y. Gu, and S. Su (2013b), Cloud-Aerosol-Radiation (CAR)
633 ensemble modeling system: Overall accuracy and efficiency, *Adv. Atmos. Sci.*, 30(4),
634 955-973, doi:10.1007/s00376-012-2171-z.
- 635 Zhang, G. J. (2009), Effects of entrainment on convective available potential energy and closure
636 assumptions in convection parameterization, *Journal of Geophysical Research*, 114(D7),
637 D07109, doi:10.1029/2008jd010976.
- 638

639 Figure Captions

640

641 **Figure 1.** Summer (JJA) 1989 averaged dCAPE (J kg^{-1}) from the KF parameterization for the
642 (a) Base and (b) Modified simulations, and their (c) difference (Modified – Base) field.

643 **Figure 2.** Modeled summer (JJA) 1989 averaged cloud fraction differences (Modified – Base)
644 for bulk layers designated as (a) very high (300 hPa – top), (b) high (500-300 hPa), (c) middle
645 (700-500 hPa), and (d) low (surface - 700 hPa).

646 **Figure 3.** Average annual cycle of monthly area-averaged cloud fraction for the SE U.S. from
647 the Base (dotted) and Modified (dashed) cases compared with the CERES observations (solid)
648 for the (a) high (500-300 hPa), (b) middle (700-500 hPa), and (c) low (surface - 700 hPa) bulk
649 layers. Note different scales.

650 **Figure 4.** Average annual cycle of monthly area-averaged radiation values (W m^{-2}) for the SE
651 U.S. from the Base (dotted) and Modified (dashed) simulations compared with the CERES
652 observations (solid) for (a) SW downwelling at the surface and (b) SW upwelling at TOA. Note
653 different scales.

654 **Figure 5.** Monthly area-averaged SW downwelling surface radiation (W m^{-2}) for the SE U.S.
655 region comparing modeled SW downwelling from the Base (dotted) and Modified (dashed)
656 simulations with the NARR data (solid) shown in the (a) 3-year time series of averages
657 computed over all hours (day and night) and the (b) month-averaged June 1989 diurnal cycle.
658 Note that the original NARR radiation data are archived as 3-h averages and provided at 3-h
659 intervals.

660 **Figure 6.** Climatological annual cycle of monthly-averaged SW downwelling radiation (W m^{-2})
661 at the surface from the Base (dotted) and Modified (dashed) cases compared with SURFRAD

662 observations (solid) at two measurement sites: (a) Table Mountain, Colorado and (b) Goodwin
663 Creek, Mississippi.

664 **Figure 7.** Time series for the SE U.S. of (a) month-averaged June 1989 diurnal cycle of 2-m
665 temperature, and (b) area-averaged number of days with a maximum 2-m temperature greater
666 than 90°F (32.2°C), shown for the Base (dotted) and Modified (dashed) simulations compared
667 with CFSR data (solid).

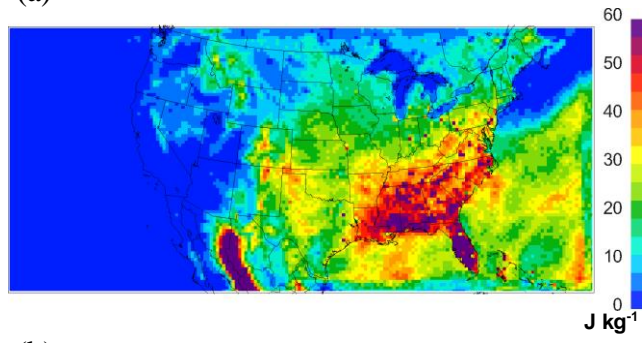
668 **Figure 8.** Summer (JJA) 1989 averaged latent heat flux (W m^{-2}) from the (a) Base and (b)
669 Modified simulations, their (c) difference (Modified – Base) field, and (d) the NARR data. Also
670 shown: Time series for the SE U.S. of (e) monthly-averaged and (f) month-averaged June 1989
671 diurnal cycle of latent heat flux from the Base (dotted) and Modified (dashed) simulations
672 compared with the NARR data (solid). Note that the original NARR latent heat data are
673 archived at 3-h intervals.

674 **Figure 9.** Time series for the SE U.S. of monthly-averaged aggregated (10 cm - 2 m) deep soil
675 volumetric moisture ($\text{m}^3 \text{m}^{-3}$) from the Base (dotted) and Modified (dashed) simulations.

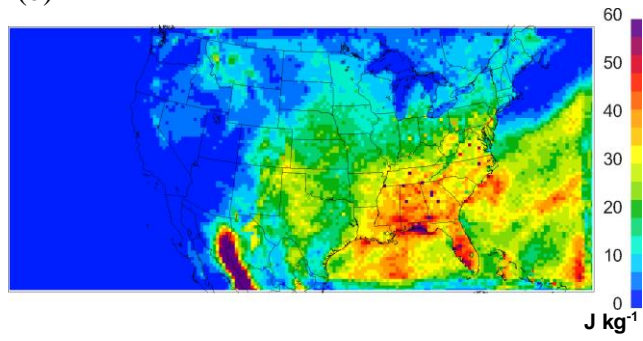
676 **Figure 10.** Time series for the SE U.S. of monthly-averaged (a) total surface precipitation (mm),
677 (b) convective surface precipitation (mm), and (c) area-averaged number of days with surface
678 precipitation greater than 1.0 inch (25.4 mm), shown for the Base (dotted) and Modified (dashed)
679 simulations compared with the NARR data (solid).

Figure 1.

(a)



(b)



(c)

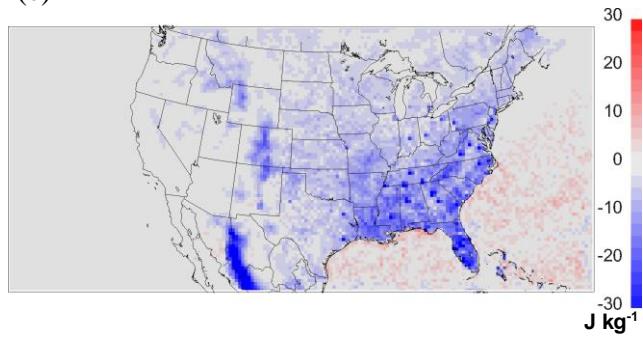
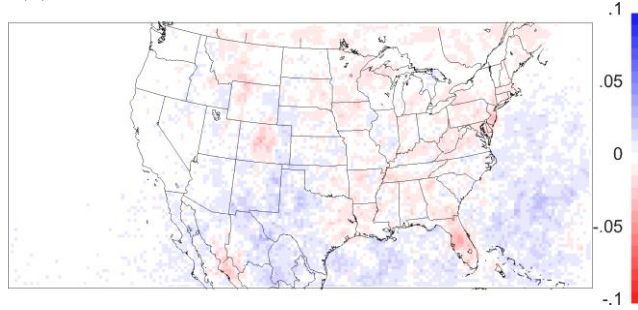
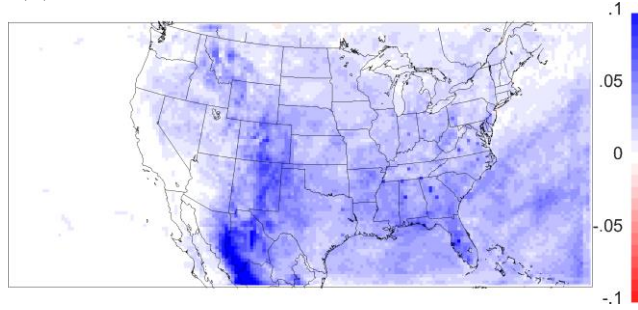


Figure 2.

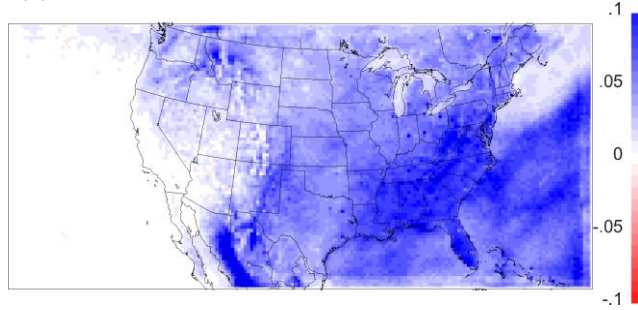
(a)



(b)



(c)



(d)

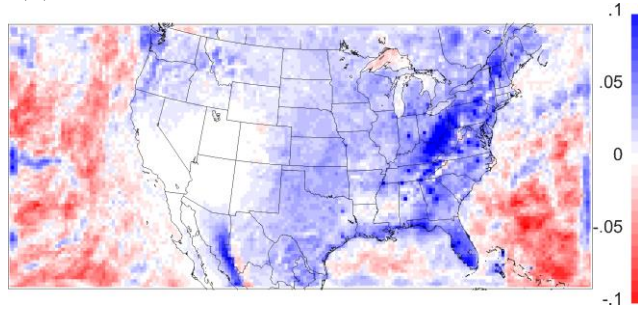


Figure 3.

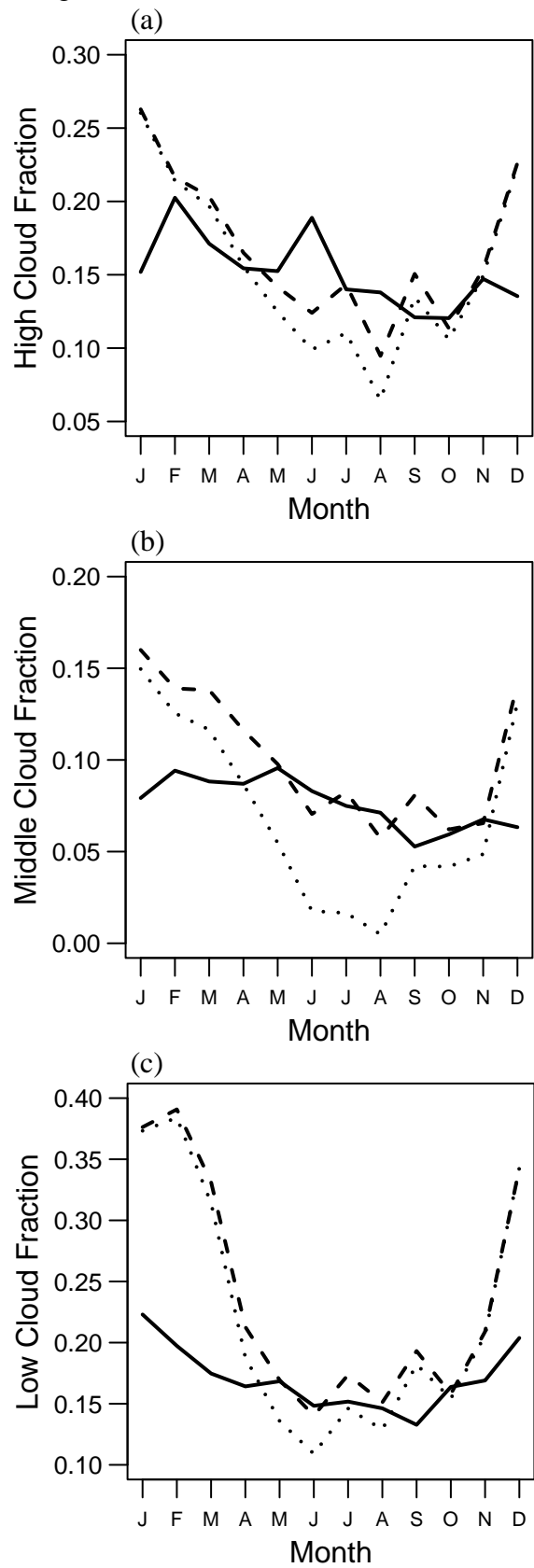


Figure 4.

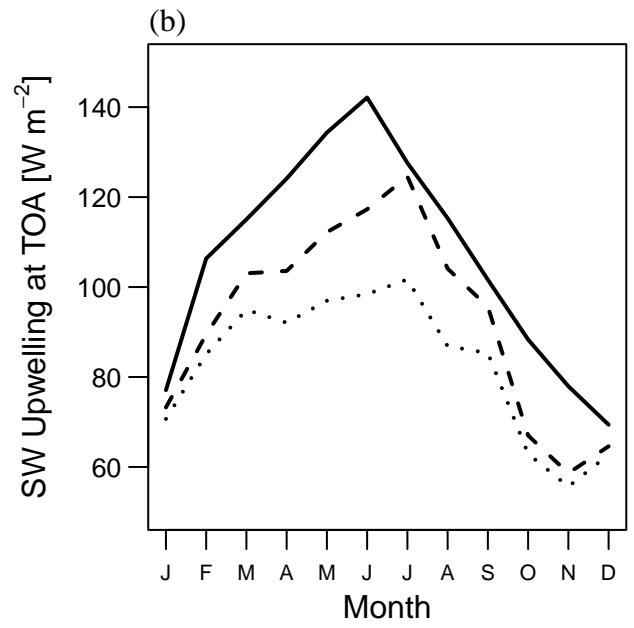
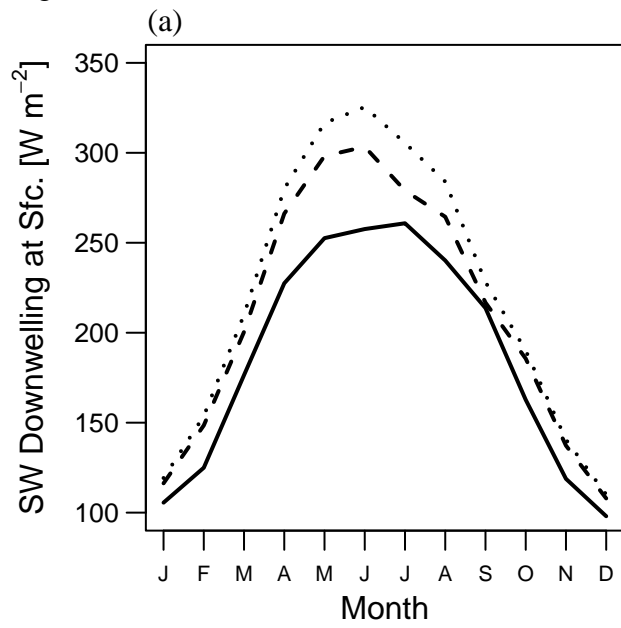


Figure 5.

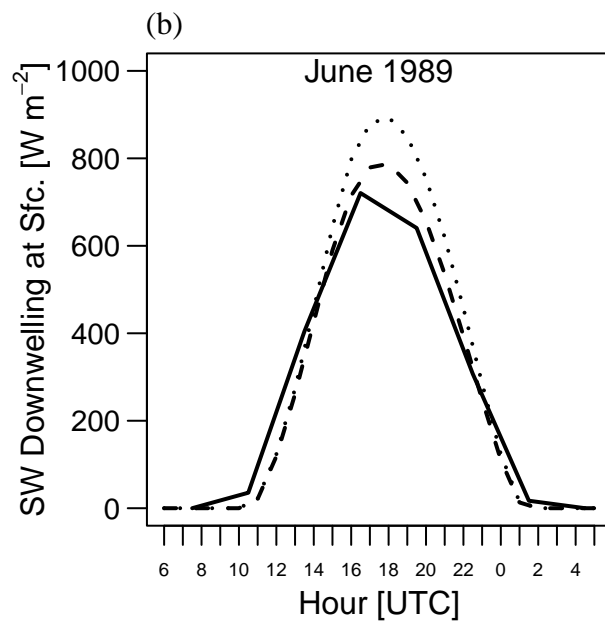
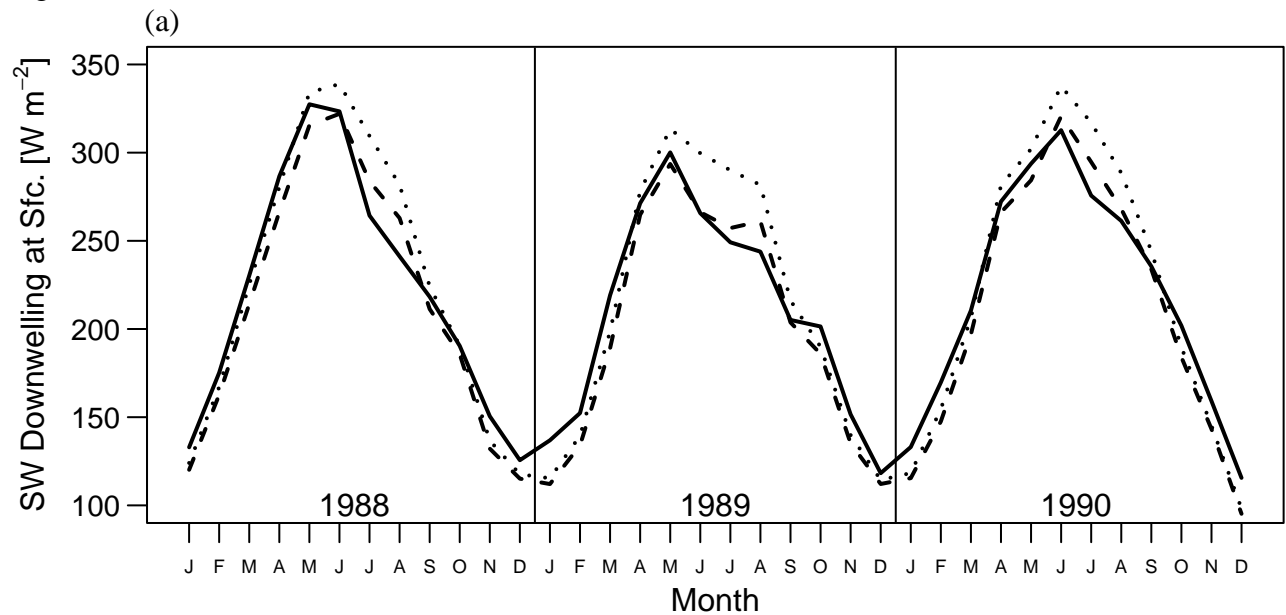


Figure 6.

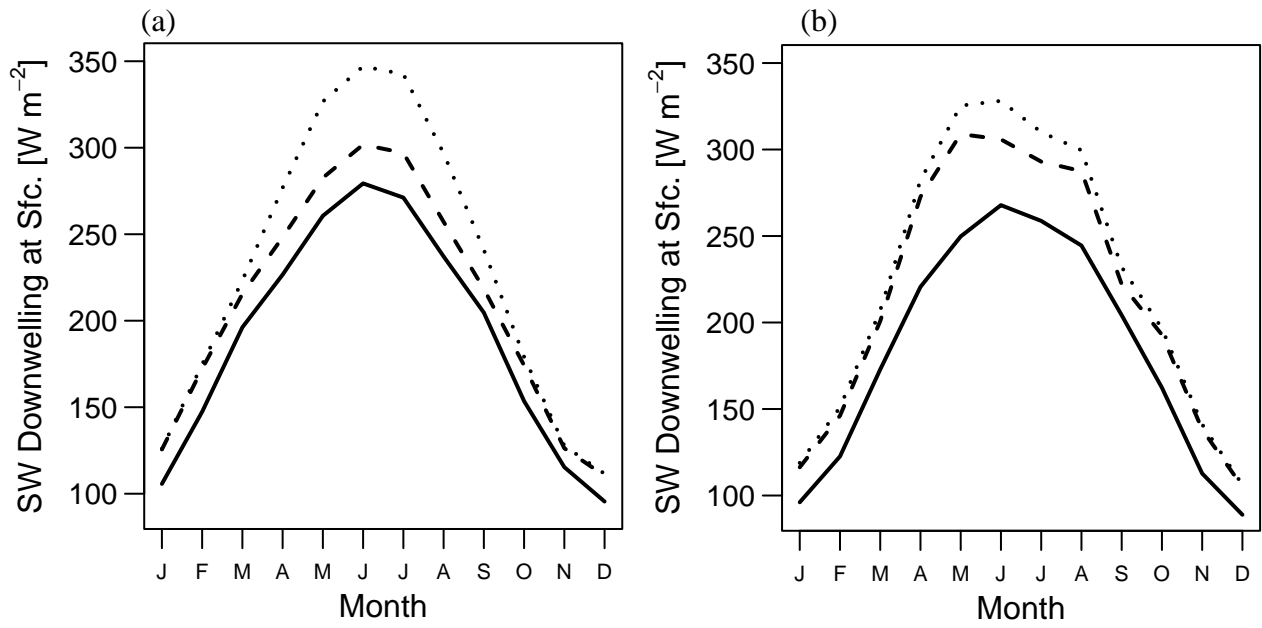


Figure 7.

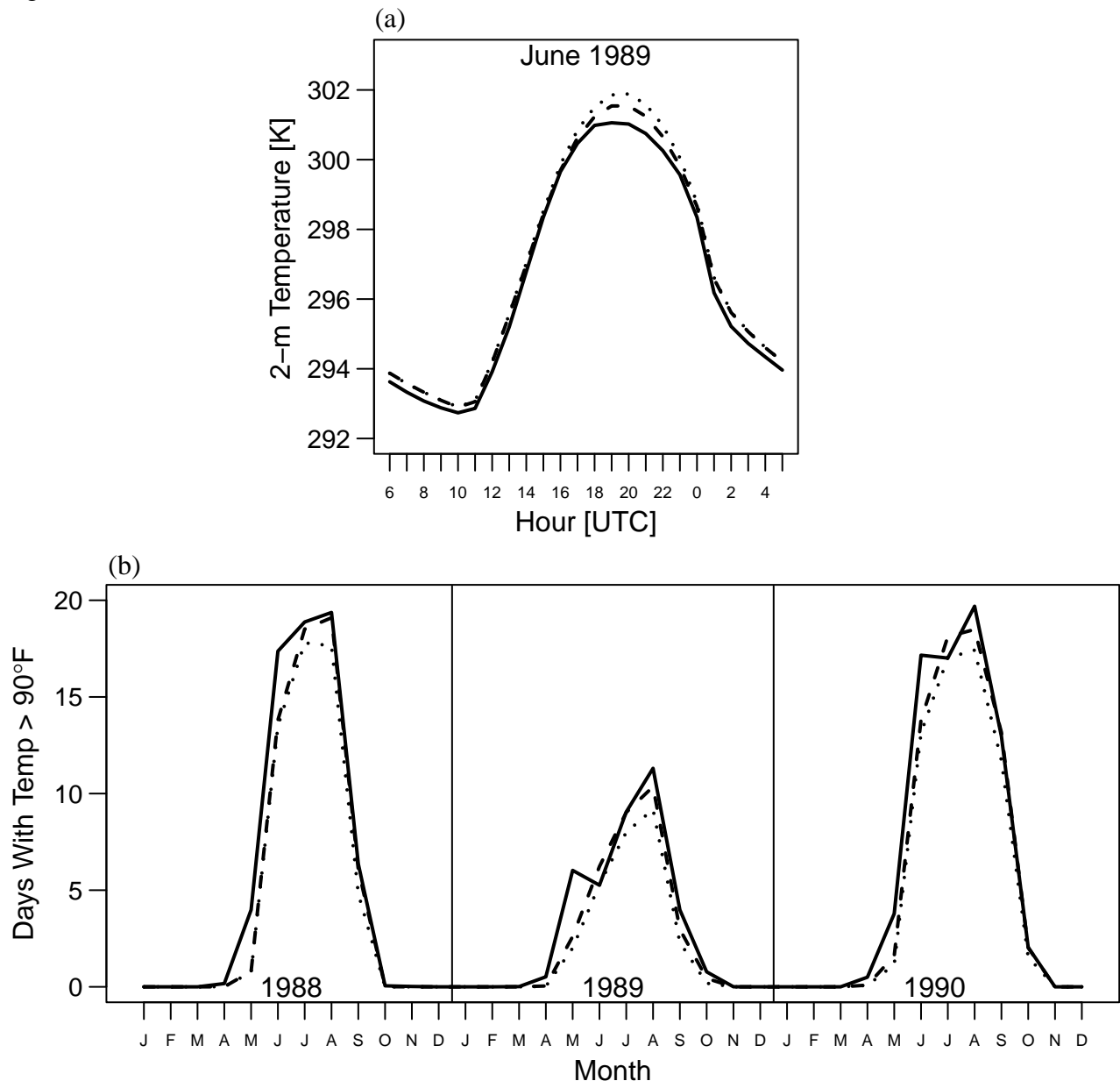


Figure 8.

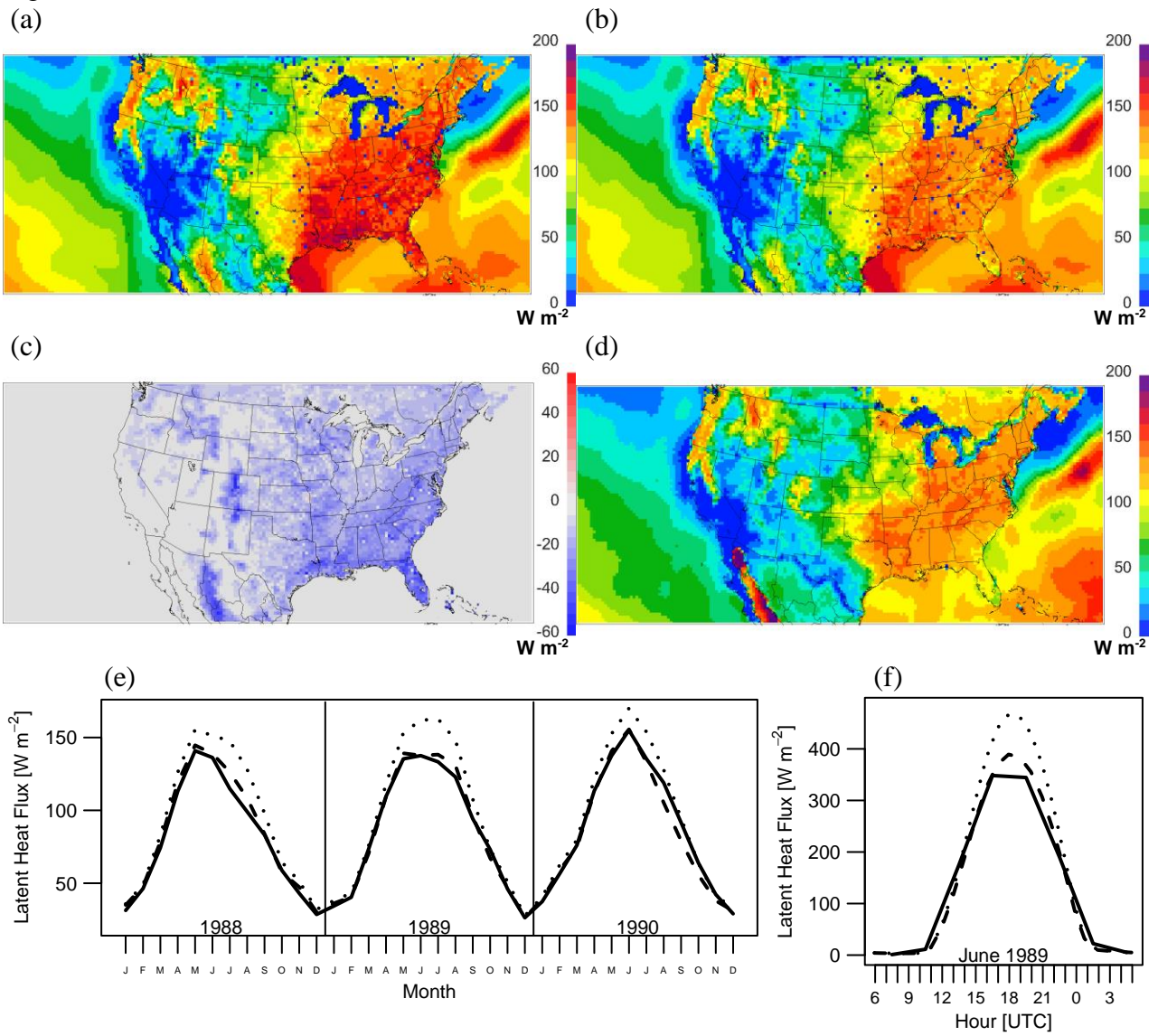


Figure 9.

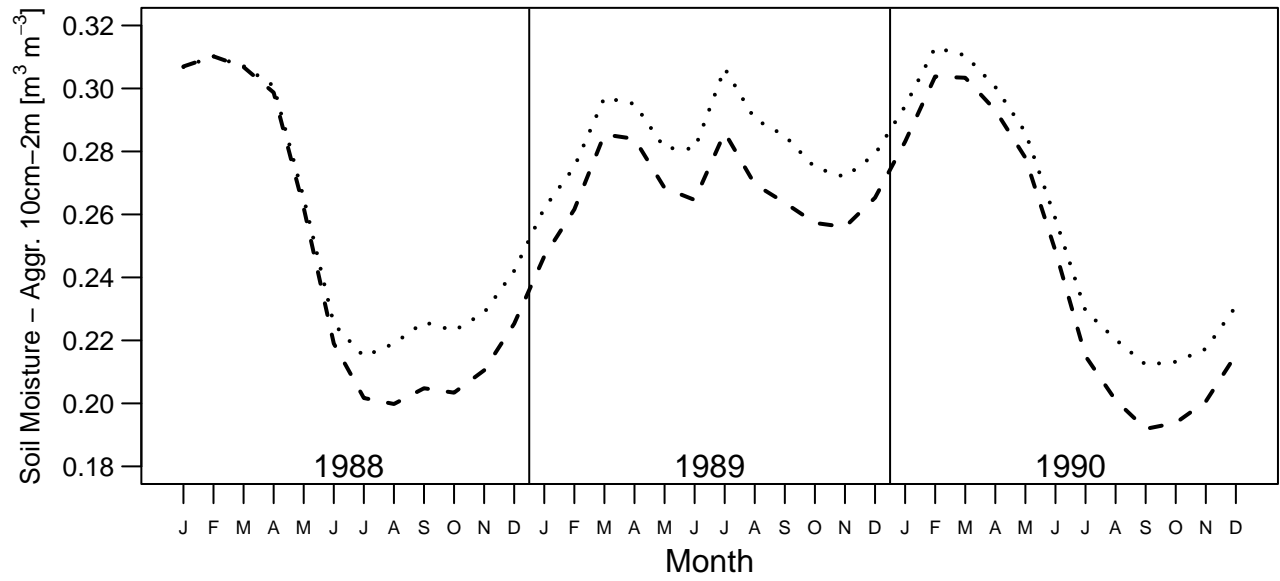
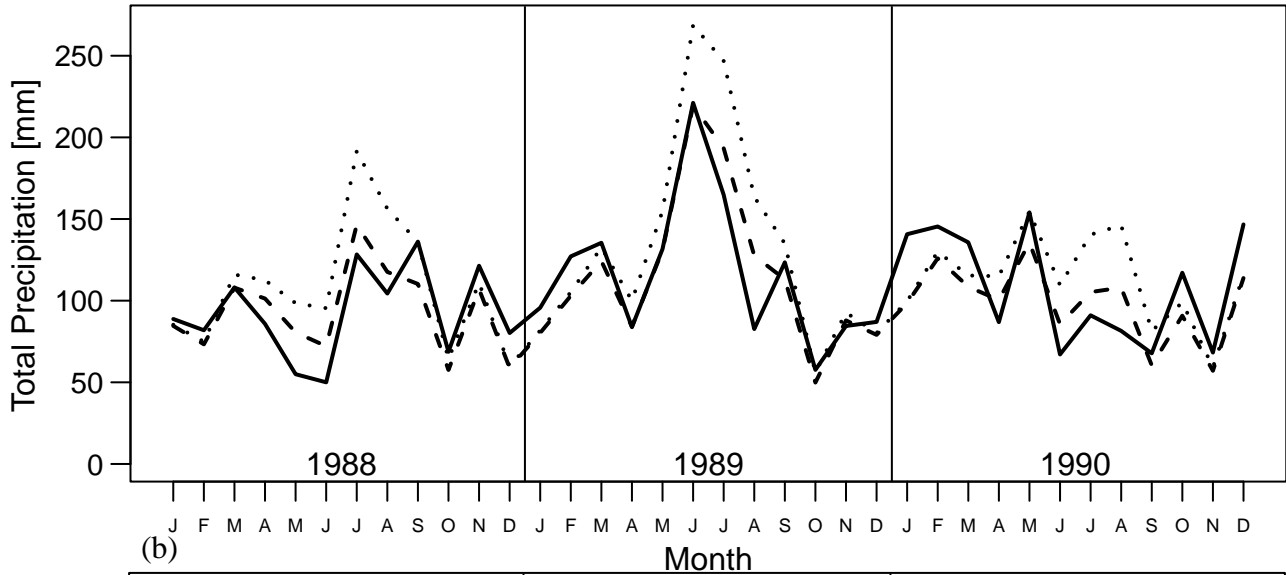
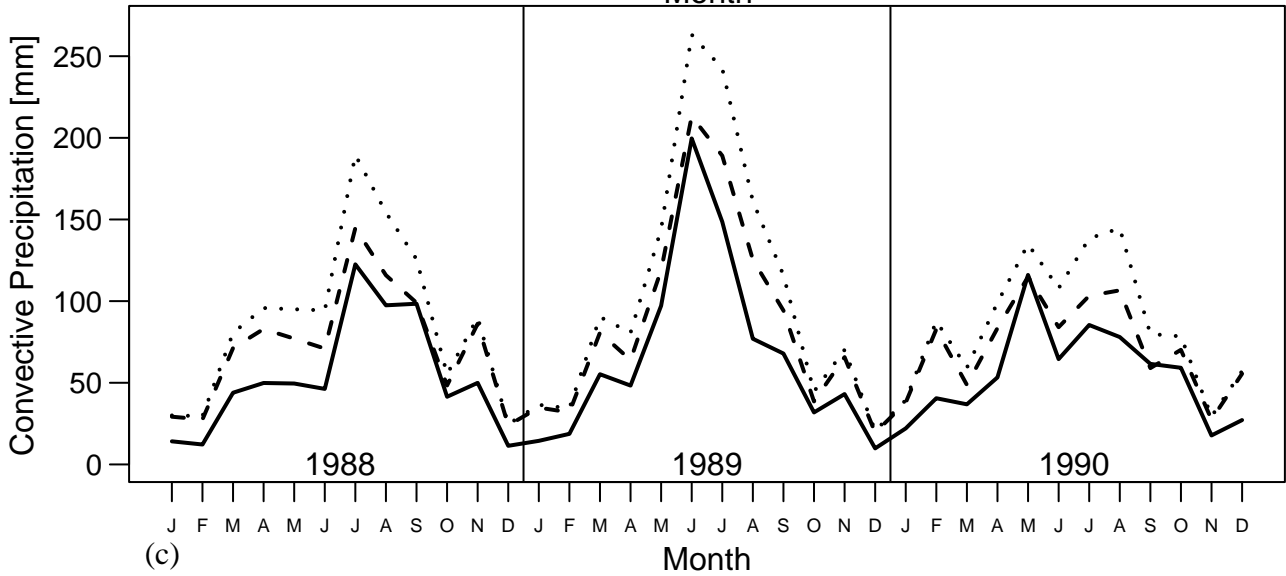


Figure 10.
(a)



(b)



(c)

